Analysis of Temperature and Pressure Fields in Molten Carbonate Fuel Cell Stacks

Joon-Ho Koh, Byoung Sam Kang, and Hee Chun Lim
Korea Electric Power Research Institute, Daejeon, Republic of Korea 305-380

A mathematical model based on fluid dynamics and heat-transfer theories was applied to predict gas dynamic pressure and temperature distribution in a coflow molten carbonate fuel cell (MCFC) stack. The mass balance was simplified to obtain exact solutions with an assumption of uniform current density in the cell. The simulations were compared with data from a pilot-scale MCFC stack. The effect of internal geometry of gas channels was simulated to accurately predict the gas-pressure drop. A close prediction of pressure drop was possible from a partially blocked gas channel model that approximates the significant flow resistance. The effect of external boundary conditions on stack temperature profile was also analyzed. Temperatures were accurately predicted from a boundary heat conduction model with a reasonable assumption of wet seal temperatures. The 2-D boundary conditions could be extended to 3-D simulations to predict temperature distribution with the same accuracy. The model was applied to see the effect of scale-up on the maximum temperature rise and average cell potential. The result verified a significant effect of cell size on the maximum stack temperature.

Introduction

Molten carbonate fuel cell (MCFC) technology has already reached a commercial scale by showing cells of 1 m^2 electrodes and a megawatt-capacity stack, but the short cell lifetime and high cost do not make it competitive in power industry. The goals of most MCFC researchers and developers at the present time are to extend cell life with a stable performance and make the system more efficient. The efforts to realize these goals are ongoing in all aspects of research fields: finding new materials, better understanding of electrochemical kinetics, innovative design of stack and cell assembly, and reliable stack operation with efficient system configuration. Mathematical modeling and simulation tools will assist many parts of development issues, especially stack design and operation. Unlike other fuel cell types, such as solid oxide or polymer electrolyte membrane fuel cells, the use of a highly corrosive electrolyte exposed to susceptible metals and oxides makes an MCFC stack more sensitive to its temperature change. Thermal management is especially important in the MCFC stack operation for this reason. Our study concerns two operating variables, temperature and gas pressure, which influence stack performance and stable operation. A mathematical model was developed on the basis of fluid dynamics and heat-transfer analysis, and the results were extensively compared with data from a pilot-plant scale MCFC stack.

Predictive models in the past showed the calculated results of temperature distribution from a variety of stack models. A study of heat transfer in fuel cells dates back to 1960s (Gidaspow and Baker, 1965). Baker (1969) did a thorough analysis of heat transfer in fuel cells and batteries. Wilemski (1980) derived thermodynamic relations of local heat release and electrochemical energy balance, and his study initiated many MCFC models for temperature prediction (Sampath et al., 1980; Wolf and Wilemski, 1983). Studies of electrode and cell performance models before the 1990s were reviewed by Takashima et al. (1990). Some past studies with most recent ones regarding the current and temperature distribution in MCFC stacks are summarized in Table 1. Studies of internal reforming MCFC stacks are not included in this table, since the heat balance of internal reforming stacks shows a very different pattern from that of external reforming ones. Studies of electrode kinetics with microscopic pore models are also excluded since they are beyond the scope of this study.

Table 1 shows the types of stack configuration and sizes on which researchers applied their mathematical models. Most researchers used basically the same mass and heat balance

Correspondence concerning this article should be addressed to J.-H. Koh.

Table 1a. Classification of MCFC Models (External Reforming Type Only)

Category	Description
(A) Cell/Stack type and operation	CO: Coflow type CR: Cross-flow type FL: Various flow types compared AP: Atmospheric operation PR: Pressurized operation with gas recycle
(B) Mass balance model with reactions	1. Faraday's law for cell reaction 2. Water-gas-shift reaction for anode gas 3. Convection in bulk phase 4. Not clearly specified
(C) Heat-transfer model	a. Conduction in solids b. Convection in gas phase c. Radiation from cell to separator d. Heat-transfer coefficient for interface flux e. Conjugate heat transfer for interface flux f. Isothermal case
(D) Gas-flow dynamics	1. Not considered 2. Momentum conservation equation 3. Darcy's law for flow in porous media
(E) I-V relation	a. Thermodynamic equation with irreversible losses (Eqs. 6 and 7) b. Not clearly specified
(F) Polarization or overpotential	1. Correlation from their own study 2. Correlation from other studies 3. Linear polarization model 4. Thin film cylindrical pore model 5. Not clearly specified
(G) Solution method	a. Finite difference method b. Computational fluid dynamics code c. Iteration for nonlinear algebraic equations
(H) Temperature boundary conditions	1. Not specified 2. Adiabatic condition 3. Conduction to fixed temperatures 4. Constant heat transfer coefficient 5. Others (periodic, natural convection, and so on)
(I) Major results compared	a. Current density distribution b. Temperature distribution c. Gas pressure distribution d. Average cell potential

Table 1b. Past MCFC Models (External Reforming Type Only) Classified in Table 1a

Ref	Size of Cell/ Stack Model	(A)	(B)	(C)	(D)	(E)	(F)	(G)	(H)	(I)
Sampath et al. (1980)	Single cell of 100 cm^2	CR AP	1,3	f	1	a	3	c	1	a
Wolf and Wilemski (1983)	Single cell of 94 cm^2	CR AP	1,2, 3	a,b, d	1	a	2	a	2	a,b
Kobayashi et al. (1989)	12 cells of 3,600 cm^2	CR AP	1,3	a,b d	1	a	4	a	5	a,b
Zaima (1989)	10 kW stack of 3,600 cm^2	CO AP	1,3	a,b c,d	1	a	2	a	1	b
Fujimura et al. (1992)	12 cells of 3,600 cm^2	CR AP	1,3	a,b, d	1	a	4	a	5	b
He and Chen (1995)	5 cells of 1 m^2	FL AP	4	a,b	2	b	5	b	1	b
Matsuyama et al. (1997)	20 cells of 1 m^2	CO PR	1,2 3	a,b, c,d	1	a	2	a	4	b,d
Yoshiba et al. (1998)	51 cells of 1 m^2	FL PR	1,2, 3	a,b, c,d	1	a	1	a	1	a,b
Mitsushima et al. (1998)	25 cells of 3,200 cm^2	CR PR	1,2, 3	a,b, d	1	a	1	a	1	a,b
Bosio et al. (1999)	20 cells of 7,500 cm^2	CR PR	1,2, 3	a,b, d	3	a	1	a	1	a,b
This study	20 cells of 3,000 cm^2	CO AP	1,2, 3	a,b, c,e	2	a	2	b	2,3 4	b,c

equations for cells or stacks. Calculation of flow fields from momentum balance was tried only by He and Chen (1995) and in this study. The electrochemical cell performance was estimated commonly from a potential balance with irreversible losses of overpotentials and internal cell resistance. Overpotentials, however, were evaluated differently in all the studies, as shown in the table. The maximum cell size considered for stack simulation was a commercial scale (1 m^2). Cross and coflow types were most frequently selected for the gas-flow configuration. Various types of gas-flow configuration were compared by Sato (1990), Fujimura et al. (1992), and Yoshiba et al. (1998). They concluded that the coflow type was better than others to lower a maximum stack temperature, although the cell voltage was a little higher in the cross-flow design. A choice between internal and external reforming types will be a matter of overall economics since both have been technically successful (Baker and Maru, 1997). Pressurized operations with gas recycling appear to be a promising MCFC operation technology, because cell performance is improved at elevated pressures and temperature can be controlled by the cathode gas recycle stream. The MCFC models were recently applied to pressurized operation (Matsuyama et al., 1997; Yoshiba et al., 1998; Mitsushima et al., 1998).

In this report, we will discuss the gas pressure and temperature distribution in a coflow type MCFC stack with internal manifolds and an external reformer at the steady-state atmospheric operation without gas recycling. The selection of a coflow configuration was based on a result from other studies. The external reforming MCFC stack at atmosphere seems to be a conventional type, but it has some importance for study since it gives us the intrinsic characteristics of MCFC stacks better than others. Analysis for further complicated design, such as internal reforming or pressurized stacks, should be done on the basis of thorough understanding of this prototype stack design. The external reforming stack at atmosphere has also the potential to be developed commercially, because of its simple design and operation.

Table 1 shows that the MCFC models have been applied to a variety of stack designs with different scales. Overall, previous studies seem to be inclined to show qualitative prediction for current density and temperature, and they did not discuss details of boundary conditions or quantitative accuracy. Our study aims at investigating these aspects of MCFC stack models for the prototype stack configuration. A quantitatively accurate prediction of temperature and pressure with consistency is of major interest in this study. There are also several other features of this study compared to the others in Table 1. Prediction of gas dynamic pressures and comparison with real data appears to be reported for the first time in this article. We also demonstrate one of the important issues that has not been reported previously: the effect of scale-up on temperature rise.

Model Formulation

Description of cell and stack models

The MCFC stack is shown in Figure 1. The following electrochemical reactions take place in electrodes, with ionic conduction through electrolyte (molten carbonate) at the same time.

$$(\text{Anode reaction})\ H_2 + CO_3^{2-} \rightarrow CO_2 + H_2O + 2e^- \quad (1)$$

$$(\text{Cathode reaction})\ CO_2 + \frac{1}{2}O_2 + 2e^- \rightarrow CO_3^{2-} \quad (2)$$

The cathode reaction is known to be exothermic, while the anode reaction is endothermic (Wilemski, 1981). The overall cell reaction is exothermic with a negative value of enthalpy change. In a planar type stack model, where cells are piled vertically, the overall reaction is usually considered for each cell package (anode + electrolyte + cathode)

$$(\text{Overall reaction})\ H_2 + \frac{1}{2}O_2 \rightarrow H_2O + \text{Electricity} + \text{Heat} \quad (3)$$

The cell performance is represented with cell potential and current density. The relationship between current density (i) and gas molar flux at electrodes surface for species-j (N_j) is described from Faraday's law

$$i = z_j N_j F \quad (4)$$

The electrical current flow over the total cell area (I) is obtained from an integration of local current densities

$$I = \int\int i\,dz\,dx \quad (5)$$

Cell potential (V_{cell}) is calculated from an equilibrium cell potential (E_{eq}) and irreversible losses due to cell resistance and overpotentials

$$V_{\text{cell}} = E_{\text{eq}} - i(R_{\text{ohm}} + \eta_{\text{anode}} + \eta_{\text{cathode}}) \quad (6)$$

The equilibrium cell potential is obtained from the standard cell potential (E^o) for hydrogen oxidation and gas compositions in thermodynamic equilibrium at a cell temperature. The standard cell potential can be calculated from Gibbs free energy of the reaction

$$E_{eq} = E^0 + \frac{RT}{2F}\ln\left[\frac{P_{H_2,a}\sqrt{P_{O_2,c}}}{P_{H_2O,a}}\frac{P_{CO_2,c}}{P_{CO_2,a}}\right] \quad (7)$$

Notice that a zero-current equilibrium potential (open-circuit voltage) is constant at fixed system pressure and temperature since reactant gases are not consumed. The equilibrium potential under load, however, decreases from inlet to outlet due to the change of gas partial pressures. This decrease of equilibrium potential, known as the Nernst loss, is automatically accounted for in this model by solving differential balance equations.

Cell overpotentials are the irreversible losses created from the electrochemical reactions at electrodes, and cell resistance is determined mainly from the structure and characteristics of cell components. The following empirical equations by Yuh and Selman (1991) were used for the estimation of overpotentials in our stack model

$$\eta_{\text{anode}} = 2.27\times10^{-9}\exp\left(\frac{6435}{T}\right)P_{H_2}^{-0.42}P_{CO_2}^{-0.17}P_{H_2O}^{-1.0} \quad (8)$$

$$\eta_{\text{cathode}} = 7.505\times10^{-10}\exp\left(\frac{9298}{T}\right)P_{O_2}^{-0.43}P_{CO_2}^{-0.09} \quad (9)$$

where P_j notes for partial pressure of species-j in unit of atm.

Cell resistance was expressed with the Arrhenius equation. The activation energy term was taken from the result by Wilemski (1983) who studied internal resistance of the same molten carbonate salt that we used in this study. The preexponential factor was determined from our measured cell resistance data at 650°C.

$$R_{\text{ohm}} = 0.5\times10^{-4}\exp\left[3016\left(\frac{1}{T}-\frac{1}{923}\right)\right] \quad (10)$$

The cell potential is related to stack operation variables such as temperature, pressure, and gas composition. In commercial-scale MCFC stacks, temperature is not uniform and pressure drop is significant. The equations for momentum and heat balances with mass continuity are necessary to calculate pressure and temperature fields. The mass conservation equations for each species in anode and cathode gas streams are also necessary for concentration distributions. A steady state is assumed in the following model equations

(mass continuity)

$$\frac{\partial \rho u_x}{\partial x} + \frac{\partial \rho u_y}{\partial y} + \frac{\partial \rho u_z}{\partial z} = \dot{r}_{CO_3^{2-}}$$

$$\textit{where } \dot{r}_{CO_3^{2-}} = +\frac{i}{z_{H_2}F}\cdot M_{CO_3}\cdot\frac{1}{\delta_g} \quad \textit{for anode gas}$$

$$\dot{r}_{CO_3^{2-}} = -\frac{2i}{z_{O_2}F}\cdot M_{CO_3}\cdot\frac{1}{\delta_g} \quad \textit{for cathode gas} \quad (11)$$

(momentum balance)

$$\frac{\partial \rho u_x u_x}{\partial x}+\frac{\partial \rho u_y u_x}{\partial y}+\frac{\partial \rho u_z u_x}{\partial z}=-\frac{\partial P}{\partial x}+\frac{\partial}{\partial x}\left(\mu\frac{\partial u_x}{\partial x}\right)+\frac{\partial}{\partial y}\left(\mu\frac{\partial u_x}{\partial y}\right)+\frac{\partial}{\partial z}\left(\mu\frac{\partial u_x}{\partial z}\right) \quad (12a)$$

$$\frac{\partial \rho u_x u_y}{\partial x}+\frac{\partial \rho u_y u_y}{\partial y}+\frac{\partial \rho u_z u_y}{\partial z}=-\frac{\partial P}{\partial y}+\frac{\partial}{\partial x}\left(\mu\frac{\partial u_y}{\partial x}\right)+\frac{\partial}{\partial y}\left(\mu\frac{\partial u_y}{\partial y}\right)+\frac{\partial}{\partial z}\left(\mu\frac{\partial u_y}{\partial z}\right) \quad (12b)$$

$$\frac{\partial \rho u_x u_z}{\partial x}+\frac{\partial \rho u_y u_z}{\partial y}+\frac{\partial \rho u_z u_z}{\partial z}=-\frac{\partial P}{\partial z}+\frac{\partial}{\partial x}\left(\mu\frac{\partial u_z}{\partial x}\right)+\frac{\partial}{\partial y}\left(\mu\frac{\partial u_z}{\partial y}\right)+\frac{\partial}{\partial z}\left(\mu\frac{\partial u_z}{\partial z}\right) \quad (12c)$$

(mass conservation of species-j)

$$\frac{\partial \rho u_x m_j}{\partial x}+\frac{\partial \rho u_y m_j}{\partial y}+\frac{\partial \rho u_z m_j}{\partial z}=\frac{\partial}{\partial x}\left(\rho D\frac{\partial m_j}{\partial x}\right)+\frac{\partial}{\partial y}\left(\rho D\frac{\partial m_j}{\partial y}\right)+\frac{\partial}{\partial z}\left(\rho D\frac{\partial m_j}{\partial z}\right)+\dot{r}_{j,\mathrm{cell}} \quad (13)$$

(heat balance for gas streams)

$$\frac{\partial \rho u_x C_p T}{\partial x}+\frac{\partial \rho u_y C_p T}{\partial y}+\frac{\partial \rho u_z C_p T}{\partial z}=\frac{\partial}{\partial x}\left(k_{\mathrm{gas}}\frac{\partial T}{\partial x}\right)+\frac{\partial}{\partial y}\left(k_{\mathrm{gas}}\frac{\partial T}{\partial y}\right)+\frac{\partial}{\partial z}\left(k_{\mathrm{gas}}\frac{\partial T}{\partial z}\right) \quad (14)$$

(heat balance for cell layers)

$$\frac{\partial}{\partial x}\left(k_{\mathrm{cell}}\frac{\partial T}{\partial x}\right)+\frac{\partial}{\partial y}\left(k_{\mathrm{cell}}\frac{\partial T}{\partial y}\right)+\frac{\partial}{\partial z}\left(k_{\mathrm{cell}}\frac{\partial T}{\partial z}\right)-Q_{\mathrm{rad}}+Q_{\mathrm{cell}}=0 \quad (15)$$

(heat balance for separator plates)

$$\frac{\partial}{\partial x}\left(k_s\frac{\partial T}{\partial x}\right)+\frac{\partial}{\partial y}\left(k_s\frac{\partial T}{\partial y}\right)+\frac{\partial}{\partial z}\left(k_s\frac{\partial T}{\partial z}\right)+Q_{\mathrm{rad}}=0 \quad (16)$$

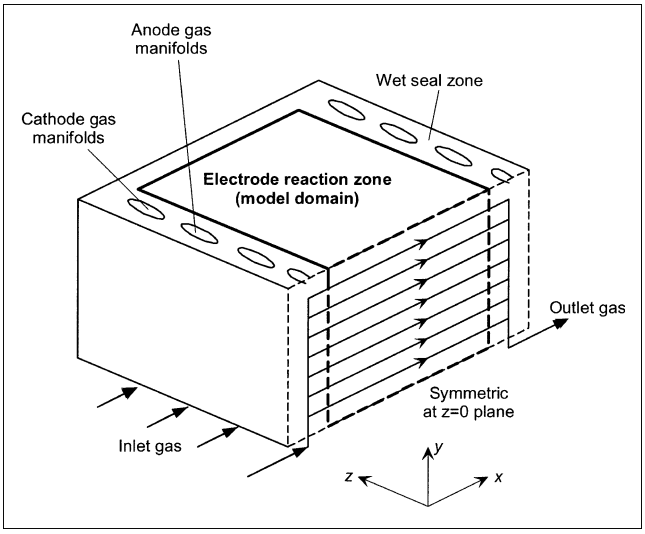

Figure 1. Coflow-type MCFC stack model with internal gas manifolds.

Equations 11 to 16 are the governing equations for 3-D simulation of flow, heat, and mass transfer in MCFC stacks. For 2-D simulation, the z-dependent terms are omitted.

Heat transfer by thermal radiation (Q_{rad}) was included in our model

$$Q_{\mathrm{rad}}=\frac{\sigma_B A_{\mathrm{cell}}\left(T_{\mathrm{cell}}^4-T_s^4\right)}{1/\epsilon_{\mathrm{cell}}+1/\epsilon_s-1} \quad (17)$$

where σ_B is the Stefan-Boltzmann constant and A_{cell} is the surface area of electrodes. T_{cell}, T_s, ϵ_{cell}, and ϵ_s denote cell temperature, separator temperature, and emissivities from cell and separator plates, respectively.

Since fuel cell is an energy conversion device, the chemical potential of reactants is converted into electricity and heat. The surface heat flux created as a result of the overall cell reaction is obtained from the thermodynamic relation of enthalpy, free energy, and entropy. The energy conversion in MCFC reactions can be represented by the standard enthalpy change (ΔH_{cell}), cell potential, and heat released (Q_{cell} or q_{cell} for surface flux).

$$q_{\mathrm{cell}}=(-\Delta H_{\mathrm{cell}})\frac{i}{z_j F}\quad -i\cdot V_{\mathrm{cell}} \quad (18)$$

Simplification of the model by assuming uniform current density

Equations 4 to 18 are a set of equations to simulate MCFC stack performance in general. All the above equations are coupled, and the calculation requires a numerical analysis with a significant amount of computation time. Two gas channels, a cell layer, and separator plates are the constituent elements of a unit cell assembly (as will be seen in Figure 5), if electrodes and electrolyte are treated as a single homogeneous cell layer. The model equations described above are applied for each cell assembly, and, therefore, the total number of equations for a typical stack having scores of cells can be huge. Simplification of the general mathematical model is desirable, depending on the main issue of investigation. When the current distribution is of major interest and the stack operation variables are considered less important, the time-consuming momentum equation can be ignored and this reduces complexity of the model significantly. If a small-area single cell is considered, temperature will be almost uniform and this eliminates the heat balances. These cases were demonstrated in the other previous studies (Table 1). In this study, our main interest is an analysis of stack operation

characteristics, focusing on the distribution of pressure and temperature. Simplifying the electrochemical aspect of the model was attempted, because the cell performance can be represented with average cell potential and power density. For this purpose, we developed a simplified model from the assumption of uniform current density over the plane of electrodes. With this assumption, the cell reaction rate is constant (zero-order reaction) for each species. The mass conservation equation in the form of Eq. 13 is then reduced to an independent differential equation for each species, and an exact analytical solution exists for a 1-D variation of gas concentrations.

The zero-order approximation of current density was studied before by Standaert et al. (1996), together with a first-order approximation. In their theoretical analysis of an isothermal fuel cell, the current density profile was originally an exponential curve, but the cell potential estimated from the zero-order and first-order approximations was not significantly different from that calculated from the exponential variation.

To derive a simplified model with this assumption, we start from Eq. 13 for mass conservation. The equation can be expressed in terms of molar flux in the gas-flow direction instead of mass flux, and the diffusion terms are dropped. Equation 11 for mass continuity is also expressed in the same way to represent a total molar flux

$$\frac{du_x y_j C}{dx} = \frac{i}{z_j F} \cdot \frac{1}{\delta_g} \tag{19}$$

$$\frac{du_x C}{dx} = \sum_j \left| \left(\frac{i}{z_j F} \right. \right. \cdot \left. \left. \frac{1}{\delta_g} \right) \right| \tag{20}$$

where u_x, y_j, C, and δ refer to axial velocity, mol fraction, total molar concentration, and gas channel depth, respectively. Notice that Eq. 20 is a summation of Eq. 19 for all the species (j) in each gas stream. Equations 19 and 20 are ordinary differential equations with x as a space coordinate. With local current density in consideration, these equations are not solved independently since they are coupled via current density (i) to other model equations. With an average current density, however, Eqs. 19 and 20 can be solved for a species molar flux ($u_x y_j C$) and the total molar flux ($u_x C$), respectively. For convenience, the following dimensionless variables are created

$$f = \frac{u_x C}{(u_x C)_{\text{in}}} \quad \text{and} \quad X = \frac{x}{L} \tag{21a}$$

$$S_j = \frac{iL}{z_j F \delta_g (u_x C)_{\text{in}}} \quad \text{and} \quad S = \sum_j S_j \tag{21b}$$

where L is the length of planar cells.

The above ordinary differential equations are then simply expressed with appropriate boundary conditions as follows

$$\frac{dfy_j}{dX} = S_j \quad y_j = y_{j,\text{in}} \quad \text{at} \quad X = 0 \tag{22}$$

$$\frac{df}{dX} = S \quad f = f_{\text{in}} \quad \text{at} \quad X = 0 \tag{23}$$

The equations are now easily solved for the dimensionless total molar flux (f) and gas concentrations (y_j). The exact solutions are functions of the dimensionless space coordinate (X), dimensionless reaction rates (S_j and S), and the inlet feed composition ($y_{j,\text{in}}$).

$$y_j = \frac{1}{f}\left(y_{j,\text{in}} + S_j X \right. \tag{24}$$

$$f = 1 + SX \tag{25}$$

The water-gas-shift reaction was taken into account in this simplified mass balance model, from the chemical equilibrium calculation of the anode feed gas composition. This reaction is known to reach a chemical equilibrium rapidly at the MCFC stack temperature in the presence of catalyst (nickel of anode)

$$\text{CO} + \text{H}_2\text{O} \leftrightarrow \text{H}_2 + \text{CO}_2 \tag{26}$$

With this simplified gas concentration model, the total number of governing equations is significantly reduced, and the numerical computation for pressure and temperature fields is much faster and more stable than the computation with the whole set of equations. Notice that the only assumption needed for this simplification is a uniform current density approximation. Equations 4 to 18 are used exactly in our model except that the differential mass conservation (Eq. 13) is replaced by the simplified concentration solution (Eq. 24).

Physical and thermodynamic parameters

Many physical and thermodynamic parameters are required for computation of the presented model. Thermodynamic data from literature were used to estimate the standard enthalpy changes of the overall cell reaction (Smith and Van Ness, 1975), and they were represented as a linear function of temperature for convenience (Figure 2). Although the enthalpy data shown in Figure 2 appear to be fitted better with a second-order polynomial function of temperature, the

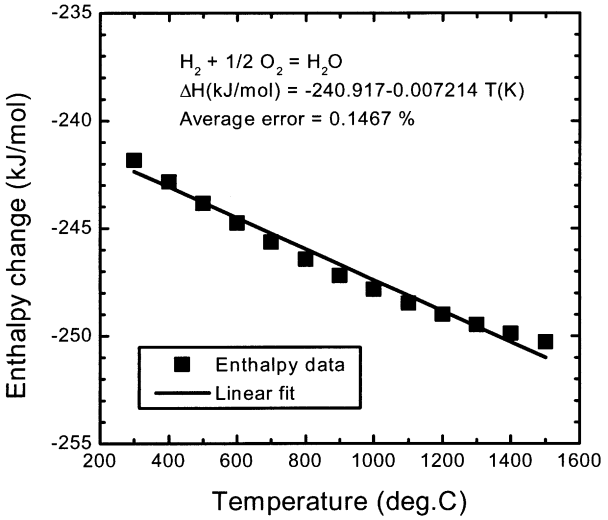

Figure 2. Enthalpy change of the overall fuel cell reaction as a function of temperature and a comparison with the best linear fit.

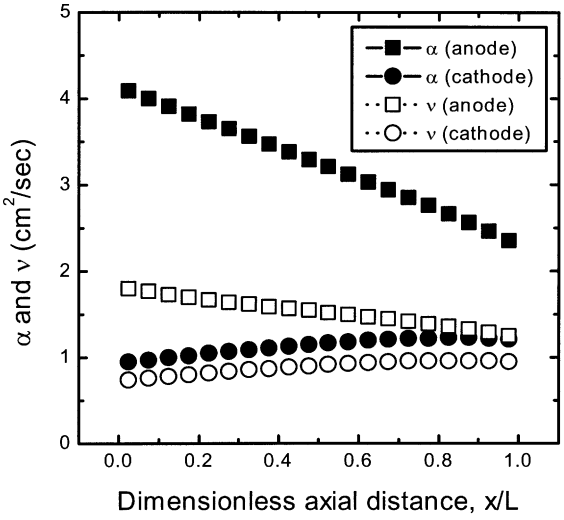

Figure 3. Axial variation of thermal diffusivity and kinematic viscosity of gas mixtures at the standard cell operating condition (150 mA/cm^2).

linear fitting is also satisfactory as the average error is only 0.15%. The chemical equilibrium constant for the water-gas-shift reaction (K_{shift}) was also expressed as a polynomial function of temperature from Gibbs free energy data

$$\Delta H_{\text{cell}} = -(240\,506 + 7.3835T) \quad [\text{J/mol}] \tag{27}$$

$$K_{\text{shift}} = 157.02 - 0.4447T + 4.2777\times10^{-4}T^2 - 1.3871\times10^{-7}T^3 \tag{28}$$

Gas properties required for computation of our model are density, heat capacity, viscosity, and thermal conductivity. The pure gas properties are strong functions of temperature. Some of the properties for pure gases are available from literature (Barin, 1989), and some of them can be calculated from well-known correlation. The property of gas mixtures can also be estimated from correlation (Reid et al., 1977). The correlation equations used for our model parameters are summarized in the Appendix. Both the anode and cathode gas properties in our model were calculated as functions of temperature and gas composition. Figure 3 shows a typical case of axial variation of two characteristic thermal and fluid properties which are defined below (Bird et al., 1960)

$$\alpha = \frac{k}{\rho C_p}: \quad \text{thermal diffusivity } (\text{cm}^2/\text{s}) \tag{29a}$$

$$\nu = \frac{\mu}{\rho}: \quad \text{kinematic viscosity } (\text{cm}^2/\text{s}) \tag{29b}$$

Figure 3 is the result from simulation of our stack model. Since temperature and gas composition vary in the axial direction of gas flow, the plots in Figure 3 indirectly show the effect of temperature and gas composition on these gas properties. As the figure shows, the change of thermal property (α) is more significant than the change of flow property (ν), especially for the anode gas. The cathode gas properties do not vary significantly due to the presence of an abundant inert gas (N_2). Figure 3 indicates that the use of constant gas properties may lead to a certain degree of miscalculation of heat transfer in fuel cell models.

Table 2. Properties of MCFC Cell Components and Separator Plates

Property	Separator (SS316L)	Cell components: Anode (Ni-Cr Alloy)	Cell components: Cathode (Nickel Oxide)	Cell components: Electrolyte $(Li/K)_2CO_3$
ρ (kg/m^3)	8,000	8,220	6,794	1,914
C_p (J/kg·K)	500	444	44,352	4,000
k (W/m·K)	25	25	5.5	-
ϵ (Emissivity)	0.286	0.118	0.586	-

Solid properties for the model are density, specific heat, and thermal conductivity. Unlike the gas properties which are estimated from known correlation, the solid properties are difficult to estimate. Experimental data or useful correlation are rarely found from literature for exactly matching specifications of the cell component materials. Properties for similar compounds were collected from various sources (Janz, 1967; Raznjevic, 1976; White, 1984; Peckner and Bernstein, 1987), and they are listed in Table 2. Since the model assumes a single layer for electrodes plus electrolyte, the properties for cell components were averaged to represent those for a cell package. Density and specific heat for a cell package were obtained from arithmetic mean values of anode, cathode, and electrolyte. A harmonic average value of anode and cathode was used for thermal conductivity for a cell layer, from the theory of conjugate heat transfer (Patankar, 1980) and a thermal conduction in series model (Song and Evans, 1999)

$$\frac{\delta}{k_{\text{cell}}} = \frac{\delta_{\text{anode}}}{k_{\text{anode}}} + \frac{\delta_{\text{cathode}}}{k_{\text{cathode}}} \tag{30}$$

Computation of the model for simulation of a 20-cell MCFC stack

The numerical solution domains were created for 2-D and 3-D calculations in the Cartesian coordinate. In both, the cell length (L) in the gas flow direction (x) was divided into 20 computational elements of an equal size. The stack height in the vertical direction was divided into a much greater number of elements of unequal grid spacing. Notice that the stack height is composed of many thin layers of gas channels and solid materials. Too many computational grids in the stacking direction (y) create a very large value of the length-to-height ratio of each computational element. A proper set of vertical grid spaces is obtained only by trial and error. Table 3 lists the vertical dimensions and how we divided each layer of our stack components. A single computation element was used for each gas channel depth to accelerate convergence and save the computation time. It did not affect the calculation accuracy when compared to the result with more elements.

The finite volume analysis method was used for the numerical computation (Patankar, 1980). The discrete solutions were obtained from running a computational fluid dynamics

Table 3. Thickness and Computational Grids of MCFC Cell Components and Separator Plates

	Dimension (m)	No. of Computational Grids
Upper and lower end Separator plates	0.08	5
Separator plates with thermocouples	0.01	5
Separator plates without thermocouples	0.005	3
Gas channel thickness	0.0008	1
Cell thickness (cathode + electrolyte + anode)	0.0025	3

(CFD) code, PHOENICS (version 2.2). In a typical 2-D calculation, the convergence was obtained within 5,000 sweeping iterations or much less than that in most cases. Equations 6 to 10 were used to calculate cell potential under the assumption of uniform current density. Equations 11 and 12 were used to solve for flow fields, and Eqs. 14 to 16 were used to solve for temperature. Gas composition was calculated from Eq. 24 as a function of axial position (x). Radiation heat transfer was calculated from Eq. 17, and the heat released from the cell reaction was calculated from Eqs. 18 and 27. The anode feed composition was considered to be in equilibrium of the water-gas-shift reaction, and the equilibrium composition was calculated from the feed gas temperature and an equilibrium constant (Eq. 28). The solid material properties were considered constants estimated from a variety of sources (Table 2), and the gas properties were calculated from correlation equations (see Appendix) as functions of temperature and gas composition.

Boundary conditions should be set for gas velocities, gas pressure, and temperature. Since Reynolds number is in the range of 1–10, the gas flow in the channel is expectedly a typical type of the laminar flow between parallel plates. No-slip boundary condition was made for each gas stream flowing the channel between the cell layer and the separator plate. The velocity of an inlet gas stream is automatically determined from a stoichiometric feed amount in Table 4, an inlet temperature, and a system pressure. The outlet gas pressure is set zero, to calculate gas dynamic pressure from the momentum equation (Eq. 12). On each side of a cell layer, a

Table 4. Molar Fluxes of Feed Gas Streams per Unit Surface Area of MCFC Electrodes (unit: 10^{-6} mol/cm$^2\cdot$s)

Gas Utilization	$i = 50$ mA/cm^2		$i = 100$ mA/cm^2		$i = 150$ mA/cm^2	
	Anode*	Cathode†	Anode*	Cathode†	Anode*	Cathode†
0.2	1.799	4.380	3.599	8.760	5.398	13.14
0.3	1.200	2.920	2.399	5.840	3.599	8.760
0.4	0.8997	2.190	1.799	4.380	2.699	6.570
0.5	0.7197	1.752	1.439	3.504	2.159	5.256
0.6	0.5998	1.460	1.200	2.920	1.799	4.380
0.7	0.5141	1.251	1.028	2.503	1.542	3.754
0.8	0.4498	1.095	0.8997	2.190	1.349	3.285

*Anode feed composition: $H_2/CO_2/H_2O = 72/18/10$.
†Cathode feed composition: $CO_2/O_2/N_2 = 30/15/45$.

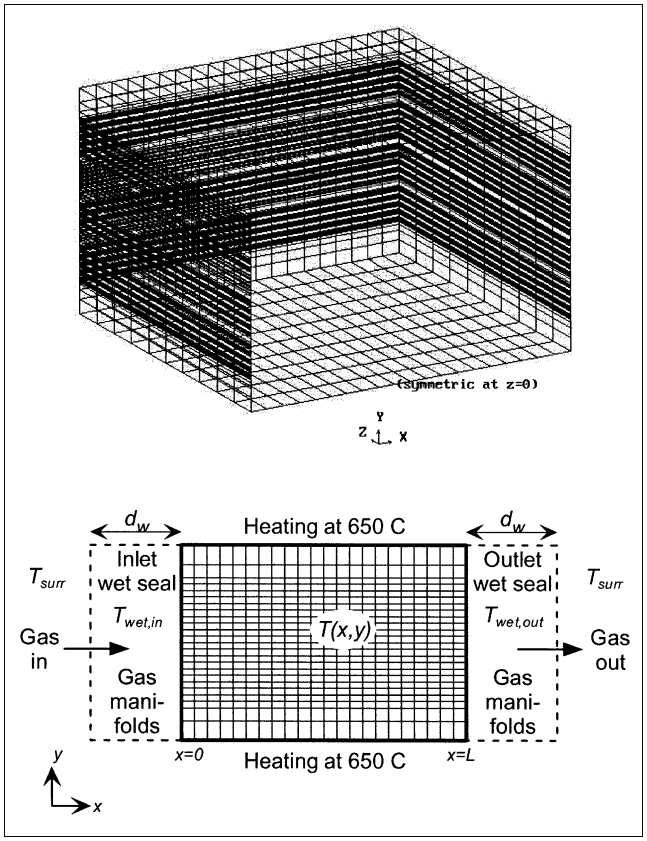

Figure 4. 3-D view of the computational grids for the model (top, created from the PHOENICS 2.2 package); 2-D view with boundary temperature boundary settings (bottom, not in real scale).

constant rate of mass change is considered with the overall mass conservation equation, as represented in Eq. 11. The gas-flow field is calculated with this set of boundary conditions. For temperature, the inside temperature distribution from cell layers to gas channels and separator plates is obtained from Eqs. 14–16, but the external heat transfer from stack to surroundings needs to be specified in advance. A description of the stack external condition is depicted in Figure 4, and more details on temperature boundary conditions are treated in the next section.

The total number of computational elements was 20×173 for 2-D simulation of our test stack described in the next section. In the 3-D model, a plane symmetry was assumed at the center of the side direction ($z = 0$) and 10 equal-spacing elements were considered from the center to the side wall resulting in a total of 20 173×10 computational grids (see the upper drawing in Figure 4). As shown in Figure 4, the vertical grids are relatively coarse near the top and bottom ends, whereas they are much denser in most of the inner layers. Figure 5 illustrates the structure of a repeating unit cell assembly and a typical flow field in the unit cell represented by two vector streams of anode and cathode. Although the model was solved for 2- or 3-D velocity components (Eq. 12), the overall velocity vector appears to be unidirectional along the

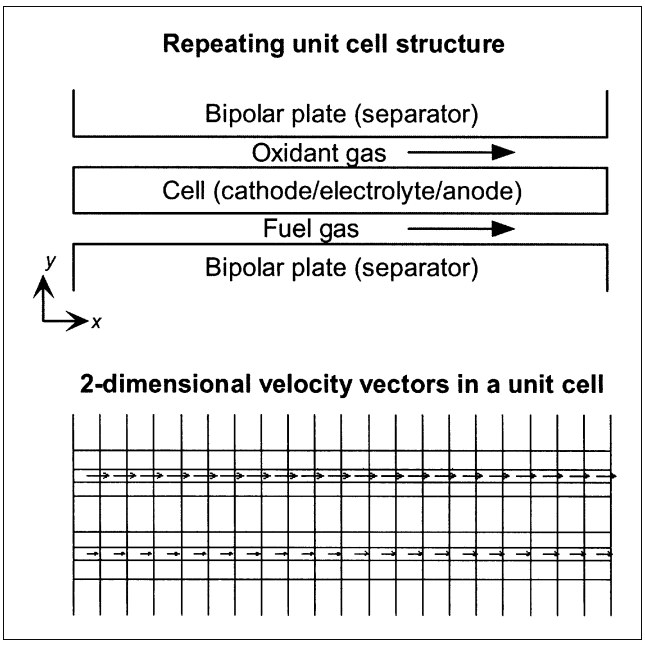

Figure 5. Repeating unit cell structure for the stack model (top) and the typical flow field from simulations represented in the unit cell grid nodes (bottom, created from the PHOENICS 2.2 package).

main flow path. The vertical grid spacing of the velocity vector field in Figure 5 was enlarged compared to the axial direction, and yet it is much smaller than the axial grid spacing.

Experimental Studies

The cell component materials are specified in Table 2. Two experimental systems were used for this study. A small single cell (100 cm^2) test system was used to collect preliminary data of cell performance and for analysis of gas composition. Temperature and pressure distributions were measured from a 20-cell stack (3,000 cm^2 cell area) with a pilot-plant scale test system. The size of each cell for this 20-cell stack was 76 cm (width) $\times$ 41 cm (length), and the matching separator plate was 82 cm $\times$ 60 cm. The extended area of the separator plates beyond the cell dimension is called the wet seal. The anode and cathode feed gases entered the stack in the same direction (co-flow), and the gas distribution to each channel on electrodes was achieved with the manifolds inside the wet seal zone (Figure 1). The top and bottom end separator plates were 80 mm thick, and the other separator plates were 5 mm thick except for a few thicker separator plates with 10 mm thickness, which were placed every five cells. These thicker (10 mm) separator plates were especially designed to allow for the insertion of 1/16 in. thermocouples to measure temperature inside the stack. The stack was heated from top and bottom electrical heating plates, and the outer surface was thermally insulated.

A dry fuel gas stream (H_2:CO_2 = 4:1) was supplied from gas cylinders and a steam methane reformer. The dry fuel gas passed a humidifier at 50°C to become a wet gas stream with about 10% water vapor. The humid fuel gas was necessary to reduce hydrogen loss by the water-gas-shift reaction and carbon deposition by a dissociation reaction. The resulting wet feed gas composition was approximately 72/18/10 (H_2/CO_2/H_2O) before the water-gas-shift reaction. The cathode gas stream was a mixture of CO_2 and compressed air at a ratio of 3:7. The stoichiometric amount of reactant gas required for a given current density is obtained from Faraday's law (Eq. 4), and the excess amount of gas is determined by gas utilization. The total molar flow rate of each feedstream is therefore determined from current density and gas utilization at the fixed feed compositions, as shown in Table 4. The inlet gas temperature to the stack was in the range of 500–580°C. Gas pressures were measured with water-filled manometers at the stack inlet and outlet for each gas stream. The stack was in operation for more than 5000 hours, but most data were collected between 1,000 and 2,000 hours of operation during which the stack showed the best and stable performance (Lim et al., 1998). A maximum instant power generated from this stack was about 7 kW at 150 mA/cm^2.

Results and Discussion

Verification of the simplified mass balance model

Our model used the simplified mass conservation model under the assumption of uniform current density and the previously known correlation for cell overpotentials. A set of cell performance and gas analysis data from a 100 cm^2 MCFC single cell was compared with calculated results from the model to validate the assumptions made. The anode gas concentrations at the cell outlet were analyzed from gas chromatography on a dry basis. The cell voltage and gas concentrations were measured from zero-load (no gas consumption) to a full load condition (15 A over 100 cm^2). The small-cell data was selected for this comparison in terms of cell voltage and gas concentration, instead of a large stack data, for a more intrinsic model validation with the minimum effect of temperature or pressure. The comparison of gas composition shown in Figure 6 gives a good agreement between data and calculated results. Although a few CO and CO_2 concentration data points show some deviation from the theoretically calculated curves, they do not significantly affect the model simulation of temperature and pressure drop. Possible reasons for the deviation are the measurement accuracy of gas concentration or a nonequilibrium state of the anode feed gas for the water-gas-shift reaction.

The total current over a plane of electrodes (I) is given as a pre-determined parameter in either a base-load operation or a load-following operation. The average cell voltage can be easily measured for a given current load. The local current density or the local cell voltage can be measured, but not easily. Most previous studies assumed a uniform cell voltage and predicted the current distribution theoretically. We assumed a uniform current density instead, for several reasons. First, the numerical computation of the models becomes simpler, due to the analytical solutions of the mass balance model under this assumption. With fluid dynamics and heat transfer coupled with others, the model has too much complexity, but the complexity is much reduced by using the exact mass balance solutions under the assumption. Second, the local cell

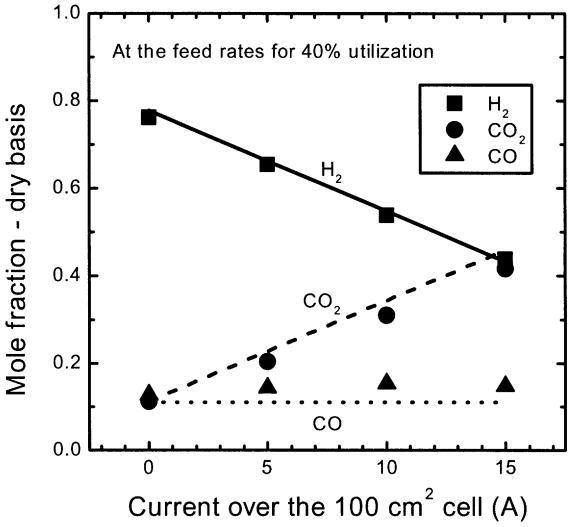

Figure 6. Calculated exit gas concentations vs. experimental data from a 100 cm^2 single cell for various electrical loads at fixed gas feed rates.

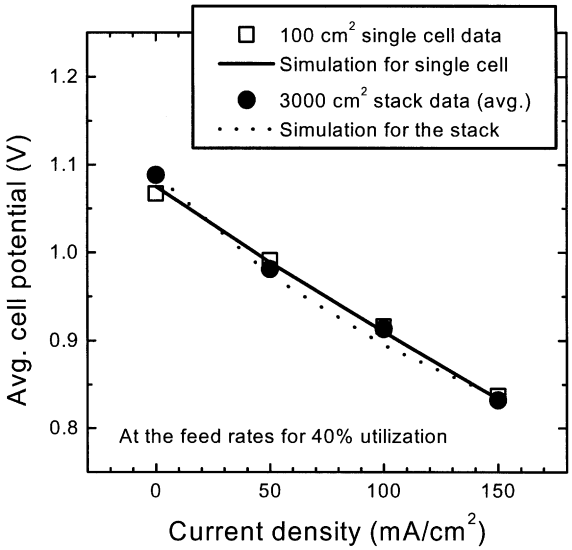

Figure 7. Calculated cell potential vs. measured data from a 100 cm^2 single cell and the kW-scale stack for various electrical loads at fixed gas feed rates.

performance can still be evaluated in terms of cell voltage from Eq. 6. The average cell voltage and total power produced are obtained as well. The model validation regarding cell performance is feasible, as shown in Figure 7.

Analysis of pressure drop across the gas channels

The molar flow rates in Table 4 are based on unit plane surface area of electrodes, and thus these values apply to any size of cell or stack, as long as the feed composition is the same as given. The feed rate for a given stack size is obtained from the tabulated values multiplied by the total reaction area and the number of cells. At the same fuel (hydrogen) and oxygen utilization, the cathode feed rate is 2.4 times higher than the anode feed rate, because the cathode gas contains a large amount of nitrogen. Practically, the MCFC system is designed to minimize fuel consumption for economic reason, while increasing the air-flow rate for stack cooling. With these design criteria, the fuel utilization is usually no less than 0.6 (60% consumption of hydrogen) and the cathode gas utilization is usually no larger than 0.4 (40% consumption of oxygen). A significant increase of cathode inlet pressure is expected, resulting in gas leak or crossover that affects cell lifetime. The maximum allowable pressure differential between cathode and anode gases is known to be ± 200 mm H_2O (~ 15 torr or 2,000 N/m^2) to prevent gas crossover.

In our 20-cell stack model, it was assumed that the flow inside the gas manifolds is uniformly distributed to all the cells in the vertical direction (y) and enters each cell uniformly in the side direction (z), since the model is concerned with the axial flow inside gas channels. The validity of this assumption will depend on manifolds design and stack height. The gas channel height was approximately 1 mm or smaller, and a value of 0.8 mm was used in our model. The internal gas manifolds have a much larger cross-section area than the gas channels, whereas the length of gas manifolds (app. 30 cm) is shorter than the gas channels (41 cm). Therefore, the pressure drop in the stack will be mostly created from the gas channels. The measured net pressure drop from stack inlet to outlet is summarized in Table 5. Each gas pressure drop was resulted from the matching feed rate in Table 4. The gas pressure data collected during the stack operation showed some fluctuation even at the same operating condition, and those at the same condition were averaged. In the model, the outlet gas dynamic pressure was set to zero (or atmosphere in terms of absolute pressure) to account for only the net pressure drop across the gas channels. The measured gas dynamic pressure at the stack outlet was in fact a little higher than zero because of flow resistance in the exhaust line mostly from pipes and valves. The data in Table 5 were obtained

Table 5. Pressure Drop from Inlet to Outlet of the MCFC Stack

	Anode Gas Press. Drop (N/m^2)			Cathode Gas Press. Drop (N/m^2)		
Gas Utilization	At 50 mA/cm^2	At 100 mA/cm^2	At 150 mA/cm^2	At 50 mA/cm^2	At 100 mA/cm^2	At 150 mA/cm^2
0.3	–	548.8	–	–	–	–
0.4	515.5	497.0	621.3	1052.5	971.6	1219.1
0.6	338.1	345.5	372.4	–	–	588.0
0.7	–	–	196.0	588.0	588.0	588.0
0.8	176.4	291.6	245.0	–	–	–

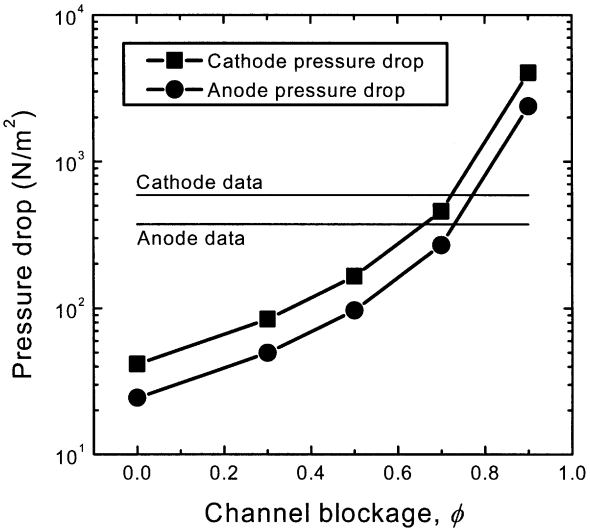

Figure 8. Simulation of the model with changing gas channel blockage (ϕ) to the fit the gas pressure drop data at 150 mA/cm^2 and 60% gas utilization in the 20-cell MCFC stack.

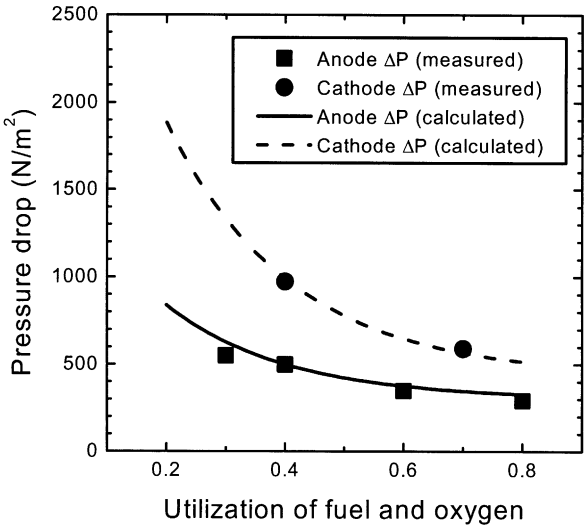

Figure 9. Prediction of gas pressure drop from the model as a function of gas utilization with ϕ = 0.7 and comparison with measured data at a constant load of 300 A over 3,000 cm^2 electrodes of the 20-cell MCFC stack.

after subtracting this outside contribution from the measured inlet pressure to result in the net pressure drop created inside the stack reaction zone.

The data at 150 mA/cm^2 with $U_f = U_{ox} = 0.6$ in Table 5 was selected for a benchmark of our model simulation. First, the model was solved assuming a fully open gas channel (no block inside). As shown in Figure 8, the calculated pressure drop at a fully open channel ($\phi = 0$) is much lower than the measured data. To fit for the data closely, it was necessary to add more flow resistance to the model. This could be done from a postulation that the gas channels are partially blocked by a volume fraction of ϕ to the total channel volume. This is another form of flow in porous media with a porosity of $(1 - \phi)$. With increasing ϕ from 0 to 0.3, 0.5, 0.7, and 0.9, the pressure fields for anode and cathode gas streams were calculated from the model, and they are compared all together in Figure 8. From the results, the calculation at $\phi = 0.7$ is very close to the data of both cathode and anode gas streams. This means the gas flow in the channel meets a drag force that is equivalent to a case when only the 30% of channel volume is open for flow path. Notice that $\phi = 0.7$ should be interpreted as a flow resistance equivalent to 70% blockage, and it does not indicate the gas channel is really occupied by certain geometrical barriers with the same volume fraction. The separator plates used for our MCFC stack were actually designed to have a certain geometry, often called ribs, inside the gas channels for uniform flow distribution, and that probably caused some flow resistance. The concept of channel blockage simplifies such a flow resistance by absorbing all different sources of flow resistance in a single parameter. A proper value of channel blockage will depend on separator design, and therefore it should be a system-dependent parameter. In our stack design, the model of a 70% channel blockage should be able to apply to predict pressure drop at other operating conditions. A set of data at 100 mA/cm^2 in Table 5 was selected for the purpose. The simulations were done at various values of gas utilization for the same current density, and the calculated result of pressure drops was compared with the data in Figure 9. The agreement is almost perfect. In spite of its simplicity, our approach to predict pressure drop works well in the specified range of stack operation.

Prediction of gas velocity and dynamic pressure profiles

With momentum equations in the model, the simulation provides us with details of stack operation characteristics such as inside profiles of pressure and velocity that we cannot measure easily. Figure 10 shows the profiles of volumetric flow rates and gas dynamic pressure in the gas flow direction. At the same utilization of cathode and anode gases for a constant current load, the volumetric flow of cathode gas is much higher than that of anode gas primarily due to the excess nitrogen. The difference of flow rate between cathode and anode decreases gradually from the inlet ($x = 0$) to the outlet ($x = L$), since the total volumetric flow rate decreases in the cathode and increases in the anode. This is because the cathode reaction consumes 1.5 mol of reactant gases and two electrons to produce a mol of carbonate ion which dissolves into the electrolyte layer and is transferred to the anode. Without gaseous product in the cathode, the total amount of reactant gases is just decreasing. The reverse is true for the anode where a mol of hydrogen fuel gas reacts with a mol of carbonate ion from electrolyte to generate two electrons and two mol of gaseous byproduct ($CO_2 + H_2O$). The same amount of mass disappears in the cathode and is created in the anode, as shown in the stoichiometric mass source or sink for each gas channel in Eq. 11. The net change of total mass in each cell is zero, because the mass consumption and production rates are balanced via ionic conduction.

The slopes of decreasing cathode flow rates and increasing anode flow rates depend on gas utilization, and they would

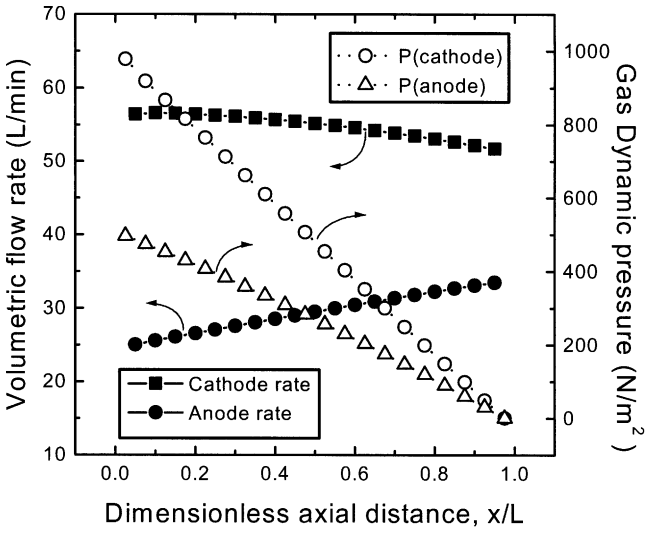

Figure 10. Axial variation of volumetric gas flow rates and dynamic pressure from simulation of the stack model at 100 mA/cm^2 and 40% utilization in the 20-cell MCFC stack.

become steeper as there are more reactions for a given feed rate (or at higher gas utilization). The gas dynamic pressures seem to be nearly influenced by the variation of volumetric gas flow rates as Figure 10 shows almost linear profiles of pressure for both cathode and anode gases.

Temperature boundary conditions

Thermodynamic evaluation with Eq. 18 shows an approximately 35% of chemical energy is converted into heat at 150 mA/cm^2. This is equivalent to a heat generation rate of about 0.07 W/cm^2 (per unit surface area of electrode plane), when the power produced is about 0.12 W/cm^2. The stack also has an external heat source to control the temperature of upper and lower end plates at 650°C. Heat released from these sources is transferred between cells, separators, or gas streams by conduction, convection, or radiation. Heat is also transferred from the stack boundary surface to surroundings, which might be called a heat loss. The boundary heat transfer seems to have been treated with a subsidiary interest in MCFC stack models. A precise description of temperature boundary condition may not be necessary for the qualitative analysis of temperature distribution. It is unlikely, however, that a more quantitative and accurate prediction of temperature fields can be done without thorough analysis of boundary conditions. The treatment of temperature boundary condition would be tricky since it is influenced by several design variables such as thermal insulation, gas flow, and wet seal. We tried several different boundary conditions and compared the calculated temperature profiles with data. Since the most significant temperature gradient is created along the gas-flow direction in the co-flow type MCFC stack, our analysis is based on temperature profiles in the axial direction from 2-D simulations on the x-y plane. The separator temperature in the middle of the stacking direction is of major interest.

The top and bottom surface ($y = H$ and $y = 0$) of the stack model is in contact with heating plates which are controlled to maintain a constant temperature (650°C). The top and bottom boundary condition is therefore expressed in general with heat conduction to/from a constant temperature heat source. When the temperature near the end separator plates is lower than 650°C, heat is supplied from the heating plate causing a positive heat flux at the surface and this is usually the case near the gas inlet of the stack.

For prediction of an accurate axial temperature profile, it is important to set up the front (inlet) and the rear (outlet) temperature boundary condition properly. We tested several different temperature boundary conditions for the stack model, and show below two most representative types among those we tried. The first type of boundary condition considers only heat conduction from the stack surface temperature $T(0,y)$ or $T(L,y)$ to a wet seal temperature T_{wet} in the middle of a wet seal distance (d_w), depicted in Figure 4. The computation domain in this case does not include wet seal, and, therefore, the model boundaries are the interface between the reaction zone and wet seal. The wet seal zone, existing uniquely in MCFC stacks, is a part of the stack with repeating layers of separator plates and ceramic porous matrices filled with liquid electrolyte. Wet seal prevents the reactant gases from leaking to outside the stack. It also provides the stack with independent anode and cathode flow regions (internal manifolds), as shown in Figure 1. These features of wet seal turn out to be important in order to set up temperature boundary condition of the first type. The heat flux at the boundary is expressed with a conduction equation

$$q_{x=0} = \frac{k}{(d_w/2)}(T_{x=0} - T_{\text{wet,in}}) \quad \text{and}$$

$$q_{x=L} = \frac{k}{(d_w/2)}(T_{x=L} - T_{\text{wet,out}}) \quad (31)$$

where $T_{\text{wet,in}}$ and $T_{\text{wet,out}}$ denote the front (inlet) and rear (outlet) wet seal temperatures. The length of seal (d_w) in our MCFC stack was about 10 cm, and the length for heat conduction in Eq. 31 is a distance from the reaction boundary to the center of wet seal (5 cm). The unknowns in this boundary condition are then two wet seal temperatures. These should be approximated on a reasonable basis. An extreme case was simulated from an assumption that the wet seal temperature is the same as boundary temperature of the reaction zone. This in fact assumes there is no heat transfer at the interface between wet seal and the reaction zone and the stack outside is adiabatic walls without a heat loss. The temperature predicted with this adiabatic wall boundary condition was too high compared to a measured temperature data, as shown in Figure 11. Apparently, there is a significant heat transfer at the reaction boundary. The next boundary condition was tried with assuming a constant wet seal temperature of 650°C. This assumption is based on the fact that the stack has an external heat source maintaining a constant temperature (650°C) and the average wet seal temperature will be largely influenced by these heaters. The wet seal zone does not have an internal heat source since there are no cell reactions, and, therefore, the wet seal temperature will not be as high as in the stack reaction zone. The predicted stack temperature with $T_{\text{wet,in}} = T_{\text{wet,out}} = 650$°C was also compared with the same data. The calculated temperature curve was much closer to the data

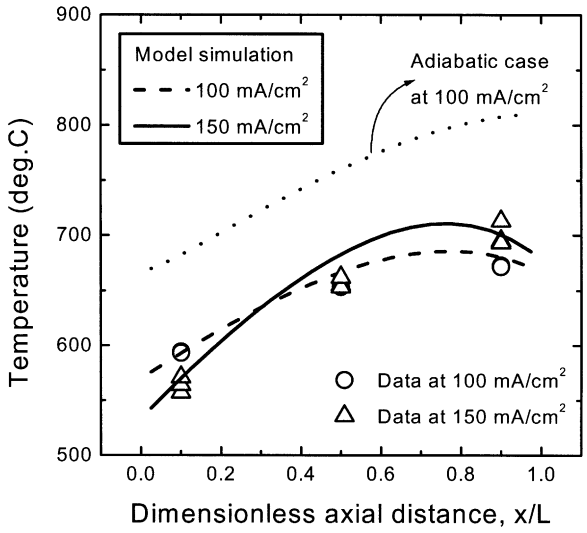

Figure 11. Axial temperature profiles from the model with the first type of temperature boundary condition (Eq. 31) and comparison with data from the 20-cell MCFC stack.

(i) 100 mA/cm^2 at 40% utilization with an inlet gas temperature of 550°C and (ii) 150 mA/cm^2 at 60% utilization with an inlet gas temperature of 500°C.

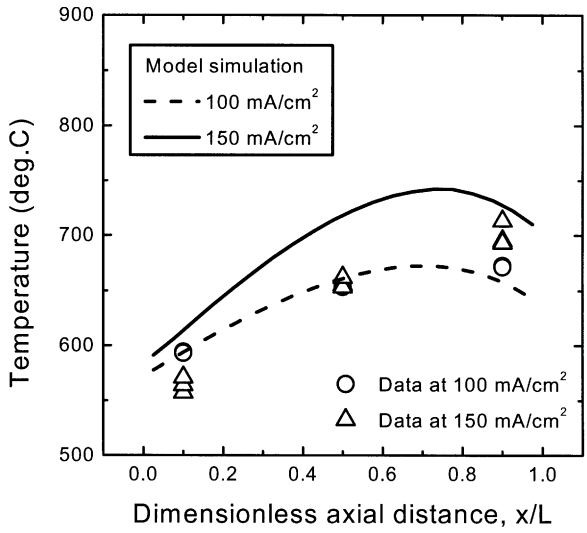

Figure 12. Axial temperature profiles from the model with the second type of temperature boundary condition (Eq. 32) and comparison with the same data as those used for Figure 11.

than the adiabatic case, but the measured temperature data were still lower than the calculation especially near the inlet. It was overlooked that the inlet wet seal temperature could be much lower than 650°C due to the relatively cold inlet gas streams flowing internal manifolds. The inlet wet seal temperature could then be assumed to be the same as the gas inlet temperature (550°C in this case). With this adjustment, the prediction agreed with the data very well, as shown in Figure 11. Figure 11 shows the application of this temperature boundary condition for temperature data measured at two different conditions: (i) at 100 mA/cm^2 with a gas utilization of 0.4 ($U_f = U_{ox} = 0.4$) and an inlet gas temperature of 550°C and (ii) at 150 mA/cm^2 with a gas utilization of 0.6 ($U_f = U_{ox} = 0.6$) and an inlet gas temperature of 500°C. The agreement is generally good in both cases.

The second type of boundary condition is one that adds an interface heat transfer from wet seal to stack surroundings to the first type boundary model. This is mathematically formulated as

$$q_{x=0} = h_o(T_{x=0} - T_{surr} \quad \text{and} \quad q_{x=L} = h_o(T_{x=L} - T_{surr} \quad (32a)$$

with

$$\frac{1}{h_o} = \frac{d_w}{k} + \frac{1}{h_{wet}} = \frac{d_w}{k} + \frac{\delta}{k_{surr}} \cdot Nu \quad (32b)$$

where δ and k_{surr} denote a characteristic length for the interface heat transfer from wet seal surface and thermal conductivity in the surrounding medium. This boundary equation eliminates the wet seal temperature from the boundary heat flux calculation. The stack outside is a thermally insulating layer, and the space between the wet seal surface and this insulation is usually filled with an inert gas. The surrounding temperature (T_{surr}) was assumed to be 400°C, based on the report by Matsuyama et al. (1997). The boundary heat flux was expressed with an overall heat-transfer coefficient (h_o), which can be obtained from a series of heat conduction through the wet seal (k/d_w) and heat convection from the wet seal surface (h_{wet}) (Bennett and Myers, 1982). The unknowns for the overall heat-transfer coefficient are δ and Nusselt number from Eq. 32b. The Nusselt number for heat transfer in MCFC stacks was reported in literature (Wolf and Wilemski, 1983; Kobayashi et al., 1989; Yoshiba et al., 1998), and they used a value in the range of $3 \sim 4$. The only unknown is then a characteristic length for the interface heat transfer from wet seal to surroundings (δ), which is hard to estimate. Stack simulations were done at various values of δ to find a value that fits most closely the measured temperature data at 100 mA/cm^2 in Figure 11. It turns out the overall heat-transfer coefficient is strongly influenced by this characteristic length. The best value of δ to fit the data was 0.2 mm. With this set of parameters, the second type boundary condition was applied to the other temperature data (150 mA/cm^2) of Figure 11. As the result shows in Figure 12, the agreement is good for the 100 mA/ cm^2 data but not good for the 150 mA/cm^2 data. The second temperature boundary model has probably some parameters which are difficult to decide, T_{surr} and h_{wet}, for instance. The physical interpretation of $\delta =$ 0.2 mm in this boundary model remains unanswered as well.

The second type temperature boundary condition using an overall heat-transfer coefficient perhaps better describes the heat-transfer mechanism at the boundary, in a physical sense, than the first type which uses thermal conductivity only. It is just difficult to use the second type for simulation in a broad operating range, because of uncertainty of stack external conditions that determine surrounding temperature and heat-transfer coefficient. The first type is simple, but easy to use, and proved to be reasonably accurate. It was the most successful boundary condition among those we tried, in terms of

fitting accuracy for our data. We would like to emphasize again that the selection of temperature boundary condition is crucial for the accurate prediction of temperature in MCFC stacks.

3-D simulation with an addition of side boundary condition

The axial and vertical profiles of temperature, pressure, and cell performance from 2-D simulations usually suffice to understand the characteristics of a co-flow type MCFC stack, although a 3-D simulation completes the whole picture of pressure and temperature fields. The 3-D simulation result gives additional information about variation of those variables in the side direction. The width of electrodes in our MCFC stack was approximately twice the length, but the variation of pressure and temperature in the side direction will be much less significant than in the axial direction. In well-designed separators and manifolds, the gas flow will be distributed uniformly from the center ($z = 0$) to the side edges ($z = \pm W/2$). Temperature will be decreasing in the same direction due to a heat loss at the side walls, although not as significant as in the axial direction. A 3-D model requires more computation elements in the z-direction, as well as the side boundary conditions. The plane symmetry can be applied. The temperature boundary condition for interface heat fluxes in the 2-D simulation can also be used for the side boundary of a 3-D model. The side wet seal temperature can be assumed a linear increase from the front wet seal temperature to the rear one (650°C). As Figure 13 shows, the linearly increasing wet seal temperature at the side boundary predicts the data well. The accuracy of prediction is quite satisfactory. The temperature boundary model that we suggested proves to be working well for 3-D simulations.

The assumption of uniform flow distribution throughout the channel cross-section would cause a debate. It is an important issue for separator design as the uniform gas distribution is necessary for stable cell performance. The flow was assumed to be uniform in this study, not because we overlooked its importance, but because the main focus of this study is confined to an analysis of axial variation.

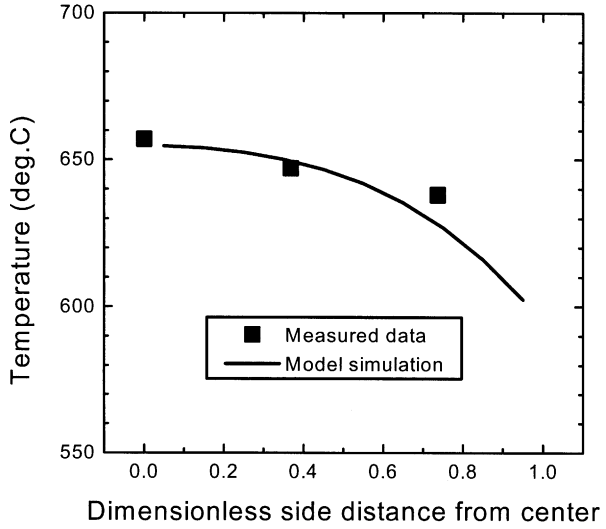

Figure 13. Temperature distribution in the side direction from 3-D simulation of the stack model and comparison with data from the 20-cell MCFC stack at 100 mA/cm^2 and 40% gas utilization with an inlet gas temperature of 550°C.

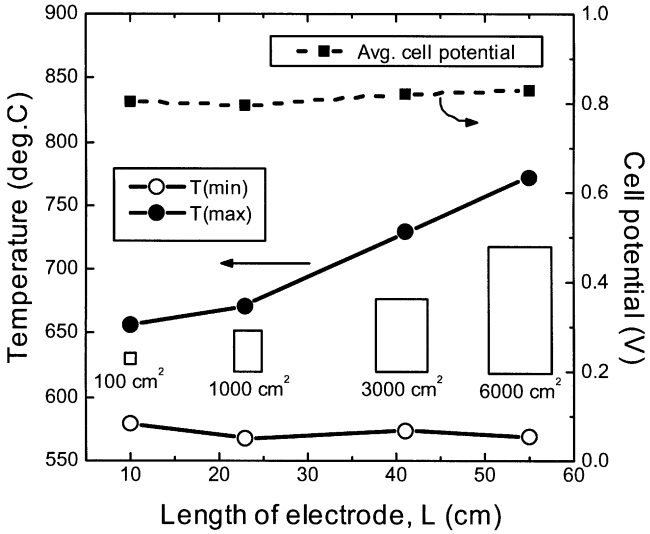

Figure 14. Effect of cell length on temperature rise and average cell voltage at 150 mA/cm^2 and an inlet gas temperature of 550°C with 60% fuel utilization and 40% oxygen utilization.

Prediction of temperature and pressure for scale-up

In the previous section, we developed the proper boundary condition to predict temperature in MCFC stacks with a reasonable accuracy. It is now applied to predict temperature in the case of scale-up. Four MCFC stack/cell models were compared in terms of average cell voltage and maximum temperature. The models include a unit cell (100 cm^2), the stack tested for this study (20 cells of 3,000 cm^2), and two others as shown in Figure 14. Temperature profiles were predicted from the model with the first type boundary condition as we stated. A relatively high fuel utilization (60%) and a lower cathode gas utilization (40%) was decided to simulate the stack operation a constant load of 150 mA/cm^2. The inlet gas temperature (550°C) was same in all the simulations compared. The maximum temperature, which appeared near the stack outlet, increases as the cell length (L) increases, as shown in Figure 14. The temperature rise does not seem to be a problem in the unit cell and the 1,000 cm^2 stack, as the maximum temperatures are slightly higher than 650°C. The largest stack in this comparison (6,000 cm^2), on the other hand, has a predicted maximum temperature of near 760°C, which will be detrimental to MCFC stack life. Obviously, special consideration of cooling is necessary for this size of stack.

The dependence of stack maximum temperature on cell size seems to be attributed to the heat transfer at stack boundaries. In spite of the different maximum temperatures, the average cell voltage remains almost unchanged in all the four stack models of different sizes, as shown in Figure 14. This indicates the stack performance in terms of power density is

not much influenced by size, while thermal management is more crucial in larger stacks.

Conclusions

The prediction of pressure and temperature was tried with mathematical models for a co-flow type MCFC stack, especially emphasizing a quantitative accuracy and consistency. For simplification of models, a set of exact solutions for mass balance in the gas phase was originally developed from the assumption of uniform current density. Cell performance and gas concentrations from this simplified mass balance model were reasonably accurate compared with measured data. Gas pressure drop could be predicted accurately with a partial blockage model of gas channels, which needs a parameter related to separator design. The use of fluid dynamics equations with the model enabled a prediction of velocity and pressure profiles. The predicted axial velocity profile reflected the intrinsic nature of mass change in MCFC precisely, by showing a decrease of volumetric flow in cathode and an increase in anode. Temperature boundary conditions were especially focused on in this study to predict the axial temperature profiles accurately. A satisfactory result was obtained for both 2-D and 3-D simulations when heat conduction to wet seal was considered at the stack reaction boundary with a properly-decided set of wet seal temperatures. The use of an overall heat-transfer coefficient from stack to surroundings resulted in the limited accuracy of temperature prediction. The temperature rise was predicted for various sizes of MCFC stack from an experimental scale to a near-commercial one. The simulations confirmed a significant effect of scale-up on temperature and almost no impact of stack size on average cell voltage.

Notation

C_p = molar heat capacity or specific heat capacity, J/mol·K or J/kg·K
D_j = diffusivity of j-species, m^2/s
F = Faraday's constant (96487 Coulomb/eqv)
h = heat-transfer coefficient, $W/m^2 \cdot K$
i = current density, A/m^2
k = thermal conductivity, W/m·K
L = cell length, m
m_j = mass fraction of species-j
$\bar{M}$ = molar average molecular weight for gas mixture, kg/mol
M_{CO_3} = molecular weight of carbonate ion, kg/mol
Nu = Nusselt number ($= h\delta/k$)
Q = rate of heat generation, W/m^3K
q = heat flux, W/m^2K
R_{ohm} = ohmic resistance, $\Omega \cdot m^2$
r_j = reaction rate in mass unit, kg/m^3sec
U_f = fuel utilization (= fuel consumption rate/fuel content of anode inlet feed rate)
U_{ox} = oxygen utilization ($= O_2$ consumption rate / O_2 content of cathode inlet feed rate)
$\boldsymbol{u}$ = velocity vector $[u_x, u_y, u_z]$, m/s
W = cell width, m
z_j = number of electrons transferred in the reaction for each species j

Greek letters

δ = thickness of a layer, m
μ = viscosity, kg/m·s
ρ = density, kg/m^3
η = impedance for electrode overpotential, $\Omega \cdot m^2$

Subscripts

cell = cell (electrodes + electrolyte in matrix)
g = gas channel
j = species index
s = separator
wet = wet seal

Acknowledgment

This work was financially supported by Korea Electric Power Corporation and R&D Management Center for Energy and Resources of The Korea Energy Management Corporation.

Literature Cited

Baker, B. S., "Heat Transfer in Electrochemical Systems," PhD Thesis, Illinois Institute of Technology (1969).
Baker, B. S., and H. C. Maru "Carbonate Fuel Cells—A Decade of Progress," *Electrochem. Soc. Proc. of the Fourth Int. Symp. on Carbonate Fuel Cell Technology*, Montreal, **97-4**, Electrochem. Soc., Pennington, NJ, 14 (1997).
Barin, I., *Thermochemical Data of Pure Substances,* VCH Verlagsgesellschaft, Weinhein, Germany (1989).
Bennett, C. O., and J. E. Myers, *Momentum, Heat, and Mass Transfer,* McGraw-Hill, New York (1982).
Bird, R. B., W. E. Stewart, and E. N. Lightfoot, *Transport Phenomena,* Wiley, New York (1960).
Blomen, L. J. M. J., and M. N. Mugerwa, eds., *Fuel Cell Systems,* Plenum Press, New York (1993).
Bosio, B., P. Costamagna, and F. Parodi, "Modeling and Experimentation of Molten Carbonate Fuel Cell Reactors in a Scale-up Process," *Chem. Eng. Sci.*, **54**, 2907 (1999).
Fujimura, H., N. Kobayashi, and K. Ohtsuka, "Heat and Mass Transfer in a Molten Carbonate Fuel Cell (Performance and Temperature Distribution in a Cell Stack)," *JSME Int. J.*, **35**(1), 82 (1992).
Gidaspow, D., and B. S. Baker, "Heat Transfer in a Fuel Cell Battery," *AIChE J.*, **11**, 825 (1965).
He, W., and Q. Chen, "Three-Dimensional Simulation of a Molten Carbonate Fuel Cell Stack Using Computational Fluid Dynamics Technique," *J. of Power Sources*, **55**, 25 (1995).
Janz, G. T., *Molten Salts Handbook,* Academic Press, New York (1967).
Kobayashi, N., H. Fujimura, and K. Ohtsuka, "Heat and Mass Transfer in a Molten Carbonate Fuel Cell (Experimental and Analytical Investigation of Fuel Cell Temperature Distribution)," *JSME International J.*, **32**(3), 420 (1989).
Lim, H.-C., B.-S. Kang, K.-S. Ahn, C.-G. Lee, J.-H. Koh, D.-H. Kim, S.-K. Kim, S.-A. Ahn, and Y.-T. Choi, "Development of a 25-kW Externally Reforming MCFC System," *1998 Fuel Cell Seminar*, Palm Springs, CA, Courtesy Assoc., Inc., Washington, DC, 194 (1998).
Matsuyama, T., A. Matsunaga, and T. Oagawa, "Prediction of Performance of Molten Carbonate Fuel Cell Stack," *Electrochem. Soc. Proc. of the Fourth Int. Symp. on Carbonate Fuel Cell Technology*, Montreal, **97**, Electrochem. Soc., Pennington, NJ, 167 (1997).
Mitsushima, S., K. Takahashi, H. Fujimura, and T. Kamo, "Lifetime Analysis Method for Molten Carbonate Fuel Cell Stacks," *Denki Kagaku*, **66**, 1005 (1998).
Patankar, S. V., *Numerical Heat Transfer and Fluid Flow,* Hemisphere, New York (1980).
Peckner, D., and I. M. Bernstein, *Handbook of Stainless Steels,* McGraw-Hill, New York (1987).
Raznjevic, K., *Handbook of Thermodynamic Tables and Charts,* Hemisphere Publishing Corporation, New York (1976).
Reid, R. C., J. M. Prausnitz, and T. K. Sherwood, *The Properties of Gases and Liquids,* 3rd ed., McGraw-Hill, New York (1977).
Sampath, V., A. F. Sammells, and J. R. Selman, "A Performance and Current Distribution Model for Scaled-up Molten Carbonate Fuel Cells," *J. Electrochem. Soc.*, **127**, 79 (1980).
Sato, S., "Development of Internal Manifolding Stack," *Electrochem. Soc. Proc. of the Second Symp. on Molten Carbonate Fuel Cell Technology*, Seattle, **90-16**, Electrochem. Soc., Pennington, NJ, 137 (1990).

Smith, J. M., and H. C. Van Ness, *Introduction to Chemical Engineering Thermodynamics (3rd Ed.),* McGraw-Hill, New York (1975).
Song, L., and J. W. Evans, "Measurements of the Thermal Conductivity of Lithium Polymer Battery Composite Cathodes," *J. Electrochem. Soc.*, **146**, 869 (1999).
Standaert, F., K. Hemmes, and N. Woudstra, "Analytical Fuel Cell Modeling," *J. of Power Sources*, **63**, 221 (1996).
Takashima, S., K. Ohtsuka, N. Kobayashi, and H. Fujimura, "Stack Performance Model of Molten Carbonate Fuel Cell," *Electrochem. Soc. Proc. of the Second Symp. on Molten Carbonate Fuel Cell Technology*, Seattle, **90**, Electrochem. Soc., Pennington, NJ, 378 (1990).
White, F. M., *Data Books: Heat Transfer and Fluid Flow,* Genium Publishing Corporation, New York (1984).
Wilemski, G., "Non-Equilibrium Thermodynamics of Fuel Cells: Heat Release Mechanisms and Voltage," *J. Chem. Phys.*, **72**, 369 (1980).
Wilemski, G., "Heat Release and EMF of Non-isothermal Molten Salt Fuel Cells," *Electrochem. Soc. Proc. of the Second Int. Symp. on Molten Salts*, Pittsburgh, **81**, Electrochem. Soc., Pennington, NJ, 385 (1981).
Wilemski, G., "Simple Porous Electrode Models for Molten Carbonate Fuel Cells," *J. Electrochem. Soc.*, **130**, 117 (1983).
Wolf, T. L., and G. Wilemski "Molten Carbonate Fuel Cell Performance Model," *J. Electrochem. Soc.*, **130**, 48 (1983).
Yoshiba, F., N. Ono, Y. Izaki, T. Watanabe, and T. Abe, "Numerical Analysis of the Internal Conditions of a Molten Carbonate Fuel Cell Stack: Comparison of Stack Performances for Various Gas Flow Types," *J. of Power Sources*, **71**, 328 (1998).
Yuh, C. Y., and J. R. Selman, "The Polarization of Molten Carbonate Fuel Cell Electrodes: I. Analysis of Steady-State Polarization Data," *J. Electrochem. Soc.*, **138**(12), 3642 (1991).
Zaima, N., "Heat Transfer Characteristics in Molten Carbonate Fuel Cell, *Electrochem. Soc. Proc. of the Symp. on Fuel Cells*, San Francisco, **89**, Electrochem. Soc., Pennington, NJ, 147 (1989).

Appendix: Gas Mixture Properties as a Function of Temperature and Composition

(1) Gas density

Assume that the gas mixture behaves as an ideal gas

$$\rho_{\text{mix}} = \frac{P\overline{M}}{RT} \tag{A1}$$

$$\overline{M} = \sum_j y_j M_j \tag{A2}$$

(2) Heat capacity

Heat capacities for the ideal gas state are independent of pressure and are functions of temperature only. The ideal gas heat capacity data were obtained from literature (Barin, 1989). The data could be expressed with a second-order polynomial equation for each component in the temperature range 298−1500 K (Table A1)

$$C_p = a + bT + cT^2 \tag{A3}$$

where C_p is in J/mol·K and T is in Kelvins.

Table A1. Constants for Ideal Gas Heat Capacities of MCFC Gases (Eq. A3)

Species	a	b	c
H_2	28.949	-5.855×10^{-4}	1.890×10^{-6}
CO_2	25.977	4.360×10^{-2}	-1.494×10^{-5}
CO	26.875	6.940×10^{-3}	-8.212×10^{-7}
H_2O	30.407	9.540×10^{-3}	1.183×10^{-6}
O_2	25.749	1.294×10^{-2}	-3.853×10^{-6}
N_2	27.313	5.190×10^{-3}	-7.212×10^{-10}

Table A2. Lennard-Jones Potential Parameters for Pure Gases

Species	σ (Å)	ϵ/k_B(K)
H_2	2.827	59.7
CO_2	3.941	195.2
CO	3.690	91.7
H_2O	2.641	809.1
O_2	3.467	106.7
N_2	3.798	71.4

The ideal gas heat capacity of a gas mixture can be calculated from the molar average of the heat capacities of the individual components (Smith and Van Ness, 1975).

$$C_{p,\text{mix}} = \sum_j y_j C_{p,j} \tag{A4}$$

(3) Gas viscosity (Reid et al., 1977)

The theory of gas viscosity is well established by applying the kinetic theory of gases. The well-known Chapman-Enskog equation applies an intermolecular potential to the elementary gas collision theory, resulting in the equation

$$\mu = 26.69\frac{\sqrt{MT}}{\sigma^2\Omega_\nu} \tag{A5}$$

where μ is in 10^{-6}g/cm·s and σ is the hard-sphere diameter in Å. The collision integral (Ω_ν) is calculated from the Lennard-Jones potential function (Table A2)

$$\Omega_\nu = \frac{A}{(T^*)^B} + \frac{C}{\exp(DT^*)} + \frac{E}{\exp(FT^*)} \tag{A6}$$

with $$T^* = \frac{k_B T}{\epsilon}$$

where $A = 1.16145$, $B = 0.14874$, $C = 0.52487$, $D = 0.77320$, $E = 2.16178$, $F = 2.43787$.

The Chapman-Enskog equation is applicable to low-pressure and high-temperature gases. The viscosity of a gas mixture is not a linear function of composition. The kinetic theory of Chapman-Enskog is extended to a low-pressure gas mixture, resulting in the expression

$$\mu_{\text{mix}} = \sum_{i=1}^{n} \frac{y_i \mu_i}{\sum_{j=1}^{n} y_j \phi_{ij}} \tag{A7}$$

where the binary interaction parameter (ϕ_{ij}) is obtained from Wilke's approximation

$$\phi_{ij} = \frac{\left[1 + (\mu_i/\mu_j)^{0.5}(M_j/M_i)^{0.25}\right]^2}{\left[8(1 + M_i/M_j)\right]^{0.5}} \tag{A8}$$

with $$\phi_{ii} = 1 \quad \text{and} \quad \phi_{ji} = \frac{\mu_j}{\mu_i}\frac{M_i}{M_j}\phi_{ij}$$

(4) Thermal conductivity (Reid et al., 1977)

Theory of thermal conduction in gases is based on the similar relations that were derived for the viscosity, but a more rigorous treatment of molecular energy is required. The well-known Eucken correlation was used for calculation of thermal conductivity of pure gases

$$\frac{kM}{\mu} = 2.25R + C_v = 1.25R + C_p \qquad \text{(A9)}$$

The thermal conductivity of a gas mixture is also a nonlinear function of composition. The equation for mixture viscosity (Eq. A7) can be used for thermal conductivity by simply substituting k for μ in Eq. A7 and calculating ϕ_{ij} from Eq. A8

$$k_{\text{mix}} = \sum_{i=1}^{n} \frac{y_i k_i}{\sum_{j=1}^{n} y_j \phi_{ij}} \qquad \text{(A10)}$$

Manuscript received Aug. 27, 1999, and revision received Jan. 8, 2001.